An optimized methane retrieval approach based on Kalman filter for mapping methane point emissions from spaceborne imaging spectrometer

Chenxi Feng[1,2], Fei Li[1,3] , Javier Roger Juan[4], Luis Guanter[4], Huilin Chen[2], Donglai Xie[5], Jun Lin[6], Lanlan Fan[6], Jianwei Cai[6], Yongguang Zhang[1,3,7]*

[1]Jiangsu Center for Collaborative Innovation in Geographical Information Resource Development and Application, International Institute for Earth System Sciences, Nanjing University, Nanjing, Jiangsu 210023, China

[2]Joint International Research Laboratory of Atmospheric and Earth System Sciences, School of Atmospheric Sciences, Nanjing University, Nanjing, Jiangsu 210023, China

[3]Jiangsu Provincial Key Laboratory of Geographic Information Science and Technology, Key Laboratory for Land Satellite Remote Sensing Applications of Ministry of Natural Resources, School of Geography and Ocean Science, Nanjing University, Nanjing, Jiangsu 210023, China

[4]Research Institute of Water and Environmental Engineering (IIAMA), Universitat Politècnica de València (UPV), Valencia, Spain.

[5]Environmental Defense Fund, Surrey, V4N0T2, Canada.

[6]China Centre for Resources Satellite Data and Application, Beijing, 100094, China

[7]Jiangsu International Joint Carbon Neutrality Laboratory, Nanjing University, Nanjing, Jiangsu 210023 China

*Corresponding author:

Yongguang Zhang (yongguang_zhang@nju.edu.cn)

February 29, 2024

Abstract

Methane (CH_4) emissions from point sources in the energy sector plays a crucial role in global CH_4 budget. Spaceborne imaging spectrometer has shown superior ability for monitoring these emission events over large spatial coverages and extended timeframes. Presently, the Matched Filter (MF), which is a data-driven method, is widely employed for satellite-based retrieval of CH_4 emission flux rates. However, traditional MF method faces challenges such as omission of CH_4 plumes and underestimation of CH_4 emission flux rate, which may lead to significant uncertainties in the CH_4 inventories for the energy industry at global scales. In this study, we propose a new Kalman-Filtering Matched Filter (KMF) algorithm as the improvement of the MF method, incorporating a linear combination of MF results in different CH_4 absorption channels to reduce the retrieval bias of point-source CH_4 enhancement values. We validate this algorithm in two stages. Retrieval accuracy for the enhancement of column-averaged dry-air mole fraction of CH_4 (XCH_4) relative to the background (ΔXCH_4) is tested using end-to-end simulation and emission-free scenario analysis. Additionally, data from hyperspectral satellites including Chinese Gaofen 5B, Ziyuan 1F, Italian PRISMA, and German EnMAP are used to retrieve CH_4 emissions from a ground-based controlled-releasing experiment using our proposed KMF and traditional MF algorithm. We then compare the retrieval results with ground metered-measurements to evaluate the performance on estimating CH_4 emission flux rate of our method. The results from end-to-end simulations show that the KMF method exhibits a 34.3% higher fitted-line slope and 25.5% lower root mean square error (RMSE) on ΔXCH_4 retrieval compared with MF method. Further analysis in an emission-free scenario indicates that the retrieval precision with the KMF method can improve by up to 42.2% compared to the conventional MF method. Comparison from controlled-releasing experiment data reveals the capability of the KMF method to detect minor CH_4 emissions that traditional MF methods fail to identify. Meanwhile, the KMF-based emission rate quantifications have an R^2 of 0.99 and a small RMSE of 0.18 ton of CH_4 per hour, which shows an approximately 62% reduction on RMSE. We further apply the KMF algorithm to Gaofen 5B and Gaofen 5 data in various regions, including the Delaware Basin (USA), Libya, Oman, and Shanxi (China) from 2021 to 2023, and focus on 16 plumes identified through case studies, highlighting the KMF algorithm's robust detection capabilities for CH_4 point source emissions in the energy industry.

Key Words

Methane point emissions; Matched filter; Kalman filter; Hyperspectral imaging spectrometer.

1. Introduction

Methane (CH_4) is the second-most abundant greenhouse gas after carbon dioxide, which has contributed to about 0.6℃ global warming since preindustrial era (Montzka et al., 2011; Shen et al., 2023). Emissions from energy sector plays pivotal role in global CH_4 inventory, constituting approximately 40% of all anthropogenic CH_4 emissions (Kirschke et al., 2013). Specifically, energy-related CH_4 emissions predominantly stem from energy-generation activities, including oil exploitation, natural gas extraction, and coal mining. These emission activities typically manifest as facility-scale point source emissions, which typically exhibit heavy-tailed distributions (i.e., small number of super-emitters contribute to a significant portion of the overall CH_4 emissions) in key energy production regions around the world (Brandt et al., 2014; Kort et al., 2014; Lyon et al., 2015). Consequently, identifying and accurately quantifying emissions from these distinct sources are essential measures in constructing precise inventories of CH_4 for global carbon budget. Furthermore, these endeavors are instrumental in enabling governments to devise tailored policies aimed at mitigating the environmental impact of CH_4 emissions.

Satellite-based remote sensing provides an efficient approach to identify and quantify energy-production-induced CH_4 super-emitters within specific geographic regions (Maasakkers et al., 2022; Pandey et al., 2019; Thompson et al., 2016; Varon et al., 2020, 2019). The presence of emission sources can be discerned through the mapping of the enhancement of column-averaged dry-air mole fraction of CH_4 (XCH_4) relative to the background (ΔXCH_4, measured in parts-per-billion, or ppb). Typically, there are two primary methodologies to derive the ΔXCH_4 map from hyperspectral radiance observations. The first approach involves full-physics methods, including Differential Optical Absorption Spectroscopy (DOAS), as discussed by Hönninger et al. (2004). The second approach utilizes data-driven methods, such as the Matched Filter (MF), as exemplified by Thorpe et al. (2013). The MF method is widely employed across various satellite data due to its high computational efficiency. For the MF algorithm, ΔXCH_4 values are estimated pixel by pixel using observed radiance, background mean radiance, radiance covariance, and CH_4 absorption spectra. Typically, the channel with stronger CH_4 absorption feature (2100-2500 nm) is mostly used during the retrieval process (e.g., Irakulis-Loitxate et al., 2021; Thompson et al., 2016; Thorpe et al., 2023). This algorithm is characterized by its simplicity in operation and relatively high accuracy, making satellite observations one of the most frequently employed methods for quantifying broad-scale and large-number CH_4 point source emissions.

Nevertheless, the traditional MF algorithm grapples with two prominent challenges. Primarily, it confronts challenges associated with false negatives, wherein it may exhibit limitations in detecting plume signals that are expected to be present, as observed using diverse satellite data. Controlled-release experiments in Wyoming, U.S. conducted by Thorpe et al. (2016) for the next-generation Airborne Visible/Infrared Imaging Spectrometer (AVIRIS-NG), an airborne hyperspectral remote sensing instrument, demonstrated an increased rate of non-retrievals corresponding to reduced emission rates using the MF retrieval strategy. For AVIRIS-NG, the false-negative rate can reach as high as 28%. In space-borne observations, the plume signal loss rate for MF retrieval results is approximately 29% (Sherwin et al., 2023a). The signal omission can be attributed to two scenarios: plume signal confusion and lost. Firstly, when the noise in retrieval results is significant, the plume signal is confounded with the background noise, making it challenging to extract the plume from background. Secondly, high values of ΔXCH_4 around emitters cannot be successfully retrieved, which shows as false negative in a scene. To solve this problem, Roger et al. (2023) suggests that incorporating information from a broader spectral range (1000-2500 nm) in the inversion process can substantially mitigate background ΔXCH_4 while maintaining signal strength within plume regions, providing theoretical underpinning for future advancements.

Furthermore, the retrieval accuracy of MF method is affected by several factors such as surface properties, non-CH_4 atmospheric compositions, etc. Ayasse et al. (2023) validates the performance of MF and DOAS methods on quantifying CH_4 emission rate using airborne hyperspectral data. Their work illustrates an overall underestimation on emission rate for MF method when compared with ground-based measurements from 2021 and 2022 controlled release experiments. Meanwhile, their results also indicate that pixel-wise DOAS inversion achieves higher accuracy in quantifying emission rates. However, the DOAS algorithm still encounters some limitations in practical applications. Due to the inclusion of a greater number of atmospheric state parameters and the iterative estimation based on forward models, the algorithm becomes time-consuming, exhibiting lower computational efficiency. This may hinder its applicability in the inversion of emissions from numerous point sources. As a trade-off of retrieval accuracy and efficiency, Pei et al. (2023) proposes an iterative MF method to improve the performance of traditional MF method. Their proposed algorithm is able to provide more accurate ΔXCH_4 estimates by progressively excluding outlier values and refining the estimation of background mean and covariance.

In this study, our objective is to propose a novel approach named Kalman filtering MF (KMF) to solve the issues of plume omission and emission rate underestimation simultaneously. The basic idea is to linearly integrate multi-bands retrieval results obtained from the MF method applied to different spectral channels and derive an optimized estimation on ΔXCH_4 values. This amalgamation of results leverages multiple CH_4 absorption features, with the goal of minimizing inversion errors and elevating the precision of CH_4 emissions retrieval. The validity of this innovative approach is assessed through comprehensive end-to-end simulation trials, observational data of metered-true CH_4 emission rates from controlled CH_4 releases experiment in 2021 and 2022, and non-emission scene tests. The results reveal that our proposed KMF method shows superior accuracy and precision for ΔXCH_4 retrieval. Finally, we apply this approach to various scenarios involving significant emitters situated in the Delaware Basin (the United States), Libya, Oman, and Shanxi (China), demonstrating its potential for CH_4 point source emission quantification on a larger scale.

2 Methods and Materials

2.1 Ground controlled-release experiment

Two ground-based controlled-release experiments are conducted by Stanford in 2021 and 2022, respectively, providing metered measurements of wind speed and emission rates with high accuracy (Sherwin et al., 2023a; Sherwin et al., 2023b). These experiments provide two datasets. One is the time series of high-precision CH_4 flux rates at the ground level. The experiment dates span from October 16th to November 3rd in 2021 and October 10th to November 30th in 2022. The other is the dataset of 10-meter wind speeds and directions above the ground. Both datasets have a temporal resolution of one second. The experiment provides references on CH_4 emission flux rates. Accuracy of inversion methods can be evaluated by comparing the retrieved emission rate against reference values.

In this study, hyperspectral radiance data from multiple satellite sensors are obtained for plume retrieval during the experiment. Table 1 exhibits the detailed technical properties of data derived from four satellite instruments (GF5B, ZY1F, PRISMA, and EnMAP). Figure 1 exhibits spatial coverages of data applied in this study. Locations of the sources in two controlled-releasing experiments is pinpointed.

Table 1. Technical parameters of four satellite sensors and data used in this study.

Satellite sensors	Swath (km)	Spatial resolution (m)	Spectral resolution (nm)	Visiting time (UTC)	Data counts	Reference
Gaofen 5-02B (GF5B) AHSI	60	30	8.5	2022-11-15 18:21	1	Irakulis-Loitxate et al., 2021
Ziyuan 1F (ZY1F) AHSI	60	30	16.8	2022-10-26 18:23	1	Song et al., 2022
PRecursore IperSpettrale della Missione Applicativa (PRISMA)	30	30	7.8-17.9 (wavelength-dependent)	2021-10-16 18:10 2021-10-21 18:10 2021-10-27 18:16 2022-10-27 18:23 2022-11-07 18:13 2022-11-30 18:09	6	Cogliati et al., 2021
Environmental Mapping and Analysis Program (EnMAP)	30	30	7.3-11.4 (wavelength-dependent)	2022-11-07 18:13	1	Storch et al., 2023

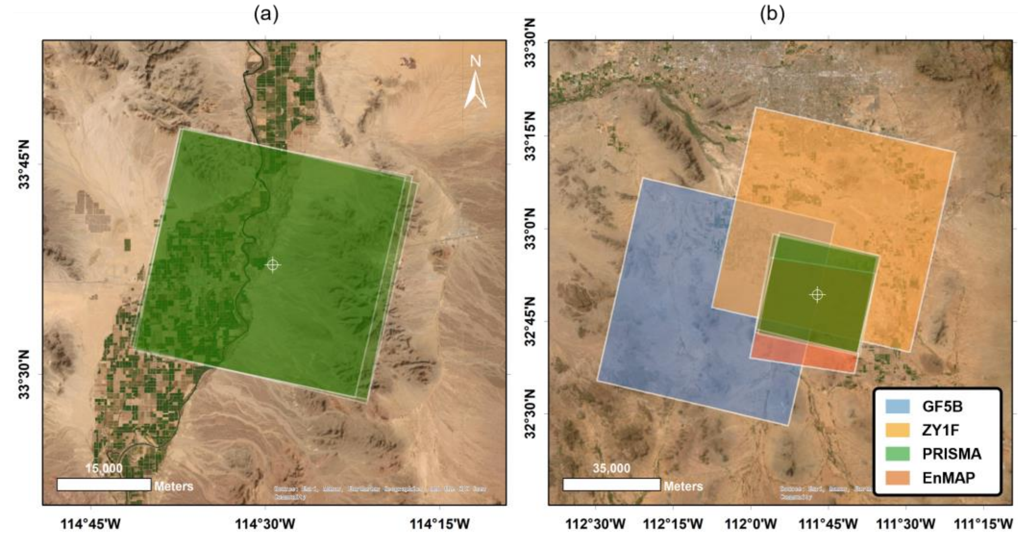

Figure 1. Spatial coverage of used data from four satellites for 2021 (a) and 2022 (b) experiments. The location of emission source is pinpointed. True-color map of the study area is from the Environmental Systems Research Institute (ESRI).

2.2 MF method

The MF method is based on Beer-Lambert's law, which reflects the exponential extinction effect of gases on radiance. Considering a ΔXCH_4 of c in the atmosphere, the radiative transfer can be modelled as:

$$\boldsymbol{x} = \boldsymbol{x}_0 \cdot e^{-c \cdot \boldsymbol{k}} \tag{1}$$

where $\boldsymbol{k}$ is the CH_4 unit absorption spectrum (i.e., the sensitivity of observed radiance to the perturbation of ΔXCH_4; Foote et al., 2020). In SWIR channel, main CH_4 absorption characteristics appear at two sub-bands (Guanter et al., 2021a). One band lies within the wavelength range of 1600 – 1900 nm, where the absorption of CH_4 on radiance is relatively weak. The other spectral region spans from 2100 to 2500 nm, exhibiting a stronger CH_4 absorption signal. The $\boldsymbol{k}$ spectrum can be generated by MODerate resolution atmospheric TRANsmission (MODTRAN; Berk et al., 2014) radiative transfer model (Foote et al., 2021). Moreover, spectral features vary from satellites due to different spectral response functions (SRF). For all four satellites, the SRFs are assumed to be in shape of Gaussian distribution and calculated using central wavelength and full width at half maximum (FWHM) of sensors (Guanter et al., 2006). Figure 2 exhibits examples for $\boldsymbol{k}$ in different spectral channels and satellites. $\boldsymbol{x}$ and $\boldsymbol{x}_0$ in Eq. 1 represent observed and reference at-sensor radiance spectrum, respectively. Top-of-atmosphere (TOA) radiance spectrum in SWIR channel is simulated using MODTRAN model, with XCH_4 set to typical background values. Responses of sensors to this spectrum are shown in Figure 3 (a). Radiance spectra in 1600-1900 nm and 2100-2500 nm channels are exhibited in zoomed-in views in Figure 3 (b) and (c). Note that there exists a missing in both $\boldsymbol{k}$ and radiance from approximately 1760 nm to 1970 nm for EnMAP data, which is due to the spectral characteristic of the sensor.

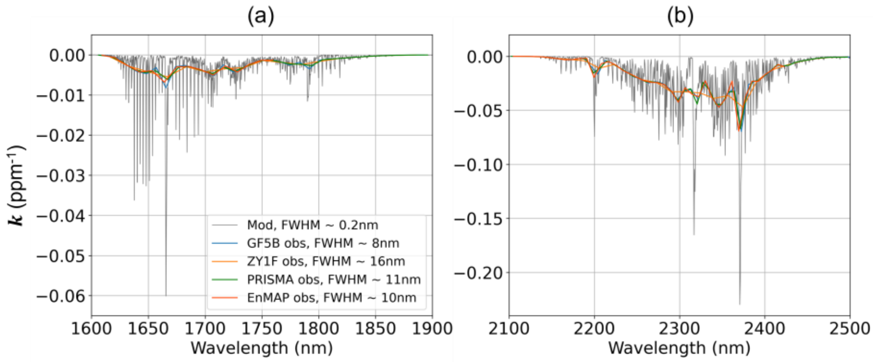

Figure 2. Samples of the $\boldsymbol{k}$ spectrum. MODTRAN outputs are shown in gray lines. Colored lines represent convolved results for different satellite sensors.

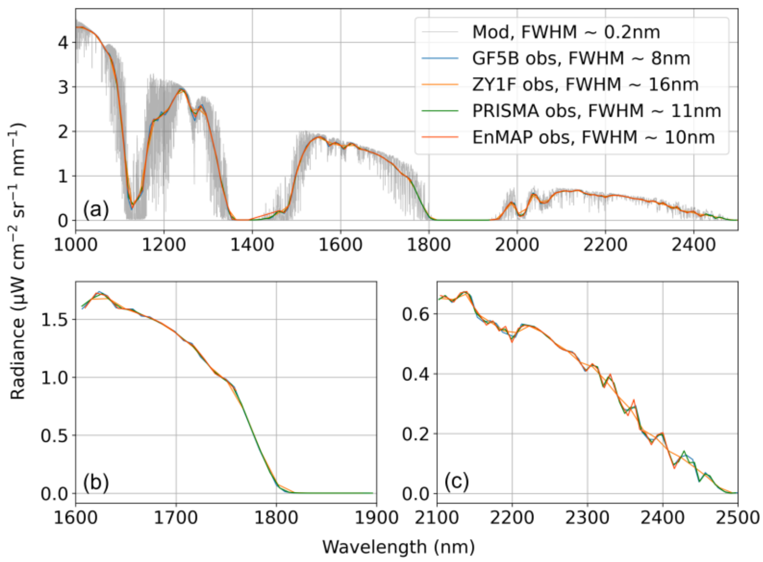

Figure 3. Synthetic radiance spectra for different instruments in (a) full SWIR, (b) 1600-1900 nm, and (c) 2100-2500 nm spectral channels. Modeled (Mod) and sensor-received results are shown in gray and colored lines, respectively. XCH_4 is set to typical background values for all simulations.

Eq. (1) can be written linearly using the first-order Taylor expansion:

$$\boldsymbol{x} \approx \boldsymbol{x}_0 + c \cdot \boldsymbol{t} \tag{2}$$

$$\boldsymbol{t} = \boldsymbol{x}_0 \odot \boldsymbol{k} \tag{3}$$

where $\boldsymbol{t}$ is the target spectrum. The background is assumed to follow a normal distribution (Manolakis et al., 2013). Thus, the noise $\boldsymbol{\eta}$ (i.e., residuals between observed and reference radiance) would obey the normal distribution with a mean of $\vec{\mathbf{0}}$ and a covariance of $\boldsymbol{\Sigma}$:

$$\boldsymbol{\eta} = \boldsymbol{x} - (\boldsymbol{x}_0 - c \cdot \boldsymbol{t}) \sim \boldsymbol{\mathcal{N}}(\vec{\mathbf{0}}, \boldsymbol{\Sigma}) \tag{4}$$

The distribution of enhanced pixels within plumes has a feature of sparsity (Foote et al., 2020).

Hence, $\boldsymbol{x}_0$ and $\boldsymbol{\Sigma}$ can be estimated by the mean ($\boldsymbol{\mu}$) and covariance of observed radiance. In this work, $\boldsymbol{\mu}$ and $\boldsymbol{\Sigma}$ are calculated column-wisely to avoid the deviation caused by the non-uniform behaviors of push-broom sensors on cross-track direction (Thompson et al., 2015). The optimal estimation of c is given by minimizing the Gaussian log-likelihood of $\boldsymbol{\eta}$ as:

$$\hat{c} = \frac{(\boldsymbol{x} - \boldsymbol{\mu})^T \boldsymbol{\Sigma}^{-1} \boldsymbol{t}}{\mathbf{t}^T \boldsymbol{\Sigma}^{-1} \mathbf{t}} \tag{5}$$

2.3 Spectral band features

Characteristics of MF-retrieved ΔXCH_4 depend largely on the spectral band applied in Eq. (5) (Roger et al., 2023a). Table 2 shows the signal-to-noise ratio (SNR) and sensitivity to ΔXCH_4 features of inversion results in different bands, which will be described in detail in the Sec. 3.2.

Table 2. Mean SNR and sensitivity to ΔXCH_4 features of retrieval results derived using three channels.

Channel	Channel name abbreviation	MF results abbreviation	Mean SNR	Sensitivity to ΔXCH_4
1600-1900 nm	WA	WAMF	High	Low
2100-2500 nm	SA	SAMF	Low	High
1000-2500 nm	SW	SWMF	Medium	Medium

For WA channel, radiance spectrum has general higher SNR values compared with the SA channel (Roger et al., 2023b). This feature enables MF retrieval applying WA channel have the potential to contain more information. However, due to a lower ΔXCH_4 sensitivity (i.e., minor changes in radiance for a unit enhancement of XCH_4), the ΔXCH_4 signal will be more difficult to be retrieved and influenced by surface variability errors using radiance in this channel (Guanter et al., 2021). On the contrary, the SW channel shows a better capability on removing the retrieval artifacts and inhibit background noise in ΔXCH_4 inversion (Roger et al., 2023a). The results derived from SA channel, which is generally used in the MF method, can provide a moderately accurate estimation of ΔXCH_4 values. However, the accuracy of retrieval based on SA channel will be impacted by measurement noise and spatial artifacts. In this study, we will demonstrate that, by integrating additional information from WA and SW spectral channels in the inversion process, it is possible to obtain a more precise estimation of enhanced CH_4 concentrations within the plume region, thereby mitigating the errors induced in single-band MF approaches.

2.4 KMF method

Here, we propose to use Kalman filter to linearly integrate multi-bands outcomes from the traditional single-band MF method. For a selected column in one scene, the strategy of band fusing is generating a linear combination of results from WA, SA, and SW bands at pixel-wise scale that is:

$$\hat{c}_{K,i} = A_{wa,i} \cdot \hat{c}_{wa,i} + A_{sa,i} \cdot \hat{c}_{sa,i} + A_{sw,i} \cdot \hat{c}_{sw,i} \tag{6}$$

where $\hat{c}_{K,i}$ is the fused result at the i-th pixel in this column. $\hat{c}_{wa,i}$, $\hat{c}_{sa,i}$, and $\hat{c}_{sw,i}$ are MF outputs at corresponding channels for this specific pixel. $A_{wa,i}$, $A_{sa,i}$, and $A_{sw,i}$ are coefficients of these bands respectively. The retrieval biases using different channels can be represented by using the spatial standard deviation σ of different channels. Then the target is to generate a combination of coefficients to minimize the σ of fusion result. As the retrieval results from different channels can be regarded as independent observations for ΔXCH_4, the optimized estimation of true values is able to be calculated using Kalman filter (Kalman, 1960) to linearly fuse results from these channels. Retrieved results from WA, SA, and SW bands correspond to three independent observations. The state and covariance prediction functions are assumed to be constant functions (i.e., true values and their uncertainty remain unchangeable across different observations). Thus, the coefficients (A_{wa}, A_{sa}, and A_{sa} for WA, SA, and SW channels respectively) can be calculated in forms of the Kalman gains to minimize the fusion result bias as:

$$A_1 = \frac{\sigma_{sa}}{\sigma_{sa} + \sigma_{wa}} \tag{8}$$

$$A_2 = \frac{\sigma_{sw}}{\sigma_{sw} + (1 - A_1)\sigma_{sa}} \tag{9}$$

$$A_{wa} = A_1 \cdot A_2 \tag{10}$$

$$A_{sa} = (1 - A_1) \cdot A_2 \tag{11}$$

$$A_{sw} = 1 - A_2 \tag{12}$$

To distinguish the enhanced CH_4 signal from the background estimation, we employed an iterative strategy based on Foote et al. (2020).The μ and Σ in Eq. (5) and Eq. (7) are updated as:

$$\boldsymbol{\mu}^n = \frac{1}{N}\sum_{i=1}^{N}[\boldsymbol{x_i} - \hat{c}_{K,i}^{n-1} \cdot (\boldsymbol{\mu}^{n-1} \odot \boldsymbol{k})] \tag{13}$$

$$\Sigma^{\mathrm{n}} = \frac{1}{N}\sum_{i=1}^{N}(\boldsymbol{d}^n)^T \boldsymbol{d}^n \tag{14}$$

$$\mathbf{d}^{\mathrm{n}} = \boldsymbol{x_i} - \hat{c}_{K,i}^{n-1} \cdot (\boldsymbol{\mu}^n \odot \boldsymbol{k}) - \boldsymbol{\mu}^n \tag{15}$$

Figure 4 shows the work flow for KMF method used in this study. Note that for PRISMA, the observation geometry parameters that needed for MF retrievals are derived from L2D data.

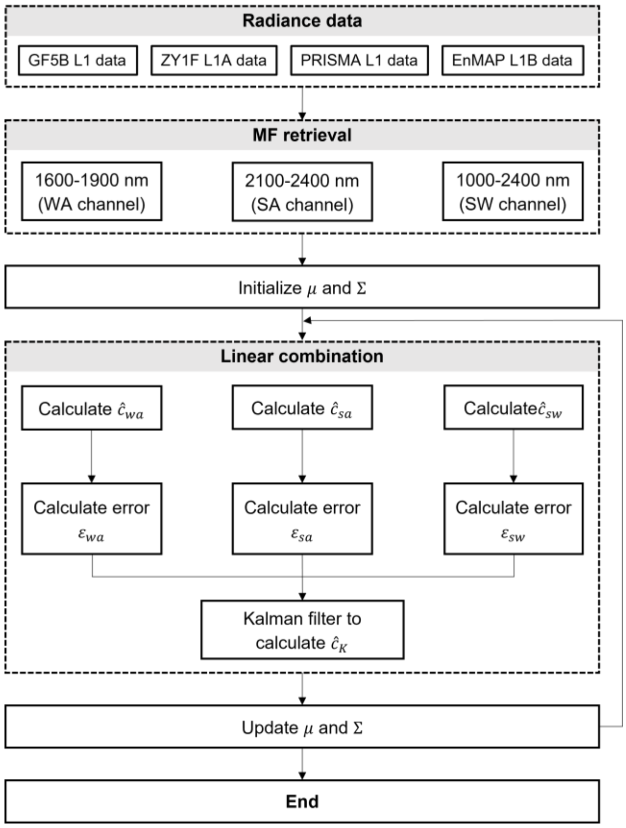

Figure 4. Flow chart of the KMF method

3 Results

3.1 Evaluation of KMF using synthetic plumes

To assess the proposed KMF method, we initially employ end-to-end simulations. Simulation of the plume from a releasing experiment on October 26th, 2022, is conducted using the Weather Research and Forecasting (WRF) in large eddy simulation (LES) mode. In order to align with satellite observations, the synthetic plume maintains a spatial resolution of 30 m. The CH_4 emission flux rate is set at a constant value of 2000 kg/h. Subsequently, this ΔXCH_4 map is transformed into a transmittance distribution using the MODTRAN model. These transmittances are then convolved with background radiance spectra obtained from an emission-free GF5B scene on September 18th, 2022 to derive the simulated at-sensor radiance spectra. Figures 5 (a) and (b) illustrate the background radiance values and simulated plume utilized in end-to-end simulation.

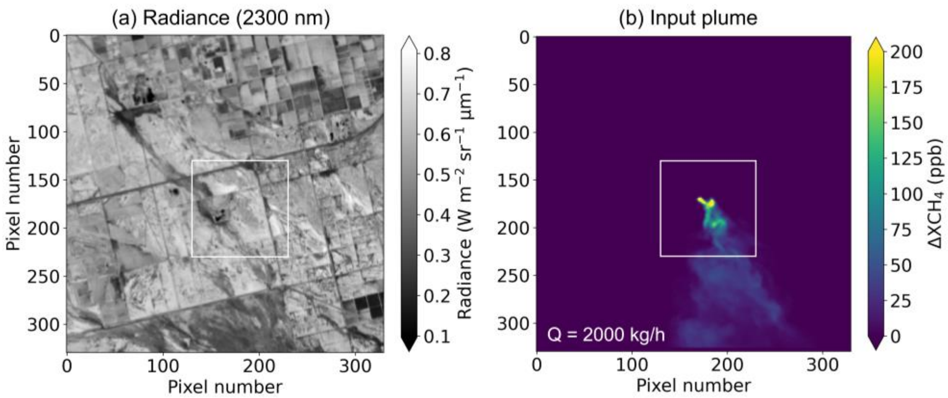

Figure 5. Samples of background radiance and input plume. (a) GF5B-received radiance at 2300 nm for an emission-free scene on September 18th, 2022. (b) Synthetic plume derived by WRF-LES as input for end-to-end simulation. White box indicates the 100×100-pixel subregion selected for analysis in this study.

Considering ΔXCH_4 values in subregion in Figure 5, the performance of the algorithm is evaluated by comparing the retrieved values with corresponding references. The results are exhibited in Figure 6. The proportional fitted line slope of KMF is 0.94, which is around 34.3% larger than widely-used SAMF (slope of 0.70) method. This reveals that KMF enables to correct the underestimation caused by SAMF method, especially for high ΔXCH_4 values. Contrary to the SAMF result, the WAMF result exhibits a slope exceeding 1 for linear fitting, indicating an overestimation. For root mean square error (RMSE, relative to input ΔXCH_4 values), the KMF method (RMSE of 32.87 ppb) enables a decrease about 25.5% compared with SAMF results (RMSE of 41.26 ppb). SWMF is the only method with a RMSE of 24.02 ppb smaller than that of KMF, but this is mainly attributed to the weaker noise in SWMF results (observable in the retrieval map) and a more concentrated distribution of background pixels. However, the notably smaller slope (slope of 0.49) in the regression line for SWMF suggests attenuation of the plume signal, introducing less retrieval accuracy. Taking all these factors into account, it can be deduced that KMF indicates the best performance on ΔXCH_4 retrieval among four approaches.

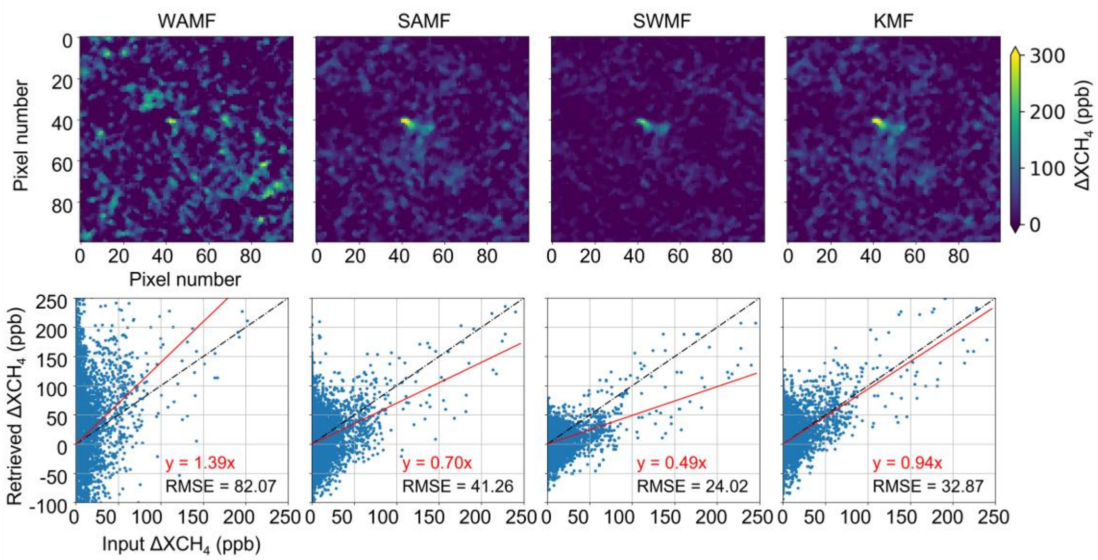

Figure 6. Comparisons of input and retrieved ΔXCH_4 values derived from different methods. First row, ΔXCH_4 maps retrieved by different methods and plume-contained subregions (white boxes) selected for analysis. Second row, scatter plots between ΔXCH_4 inversions and input values. Black dashed lines represent for 1:1 reference, while red solid lines for proportional regressions.

3.2 Validation with ground-based emission rate measurements

We further validate the KMF method using ground-based measurements from the Stanford controlled-releasing experiment held in 2021 and 2022. Radiance data collected in 9 observations from four satellites (3 scenes for 2021 experiment and 6 for 2022 experiment) are employed for CH_4 emission flux rate retrieval. With the exception of one PRISMA scene (overpassing through the emitter on Oct 27th, 2022), all datasets exhibit detected plume signals. The results for 2022 and 2021 experiments are depicted in Figure 7 and Figure S1, respectively. To avoid extra errors stemming from manual masking, we employ the strategy proposed by Roger et al. (2023). Specifically, pixels in KMF outputs surpassing the scene mean plus one spatial standard deviation (STD, σ) are identified as anomalously enhanced and attributed to the plume region. Median filter is added to eliminate artifacts near the mask boundaries. Masks for all detected plumes are illustrated in the fifth column of Figure 7. Note that the plume mask for PRISMA on Nov 7th, 2022 is not significant. This is due to the low CH_4 emission flux rate in the experiment (around 400 kg/h) resulting in small ΔXCH_4 values within the plume and making it challenging to distinguish from the background. For GF5B, ZY1F, and EnMAP, all methods are capable of identifying plume signals. The PRISMA data on Nov 7th and Nov 30th, 2022, however, fails to recognize plumes in either WA or SA channels. One type of plume missing is unclear signal distinction from background noises (e.g., WAMF values for PRISMA on Nov 7th and 30th, 2022; SAMF result for PRISMA on Nov 7th, 2022). The other is non-significant concentration enhancement signal (e.g., SAMF values for PRISMA on Nov 30th, 2022). Despite these variations, the KMF method proves effective in identifying plume signals for all four satellite sensors when compared to single-band retrieval results. It emphasizes the potential pitfalls of relying solely on single-band inversion for plume detection, which may result in omissions.

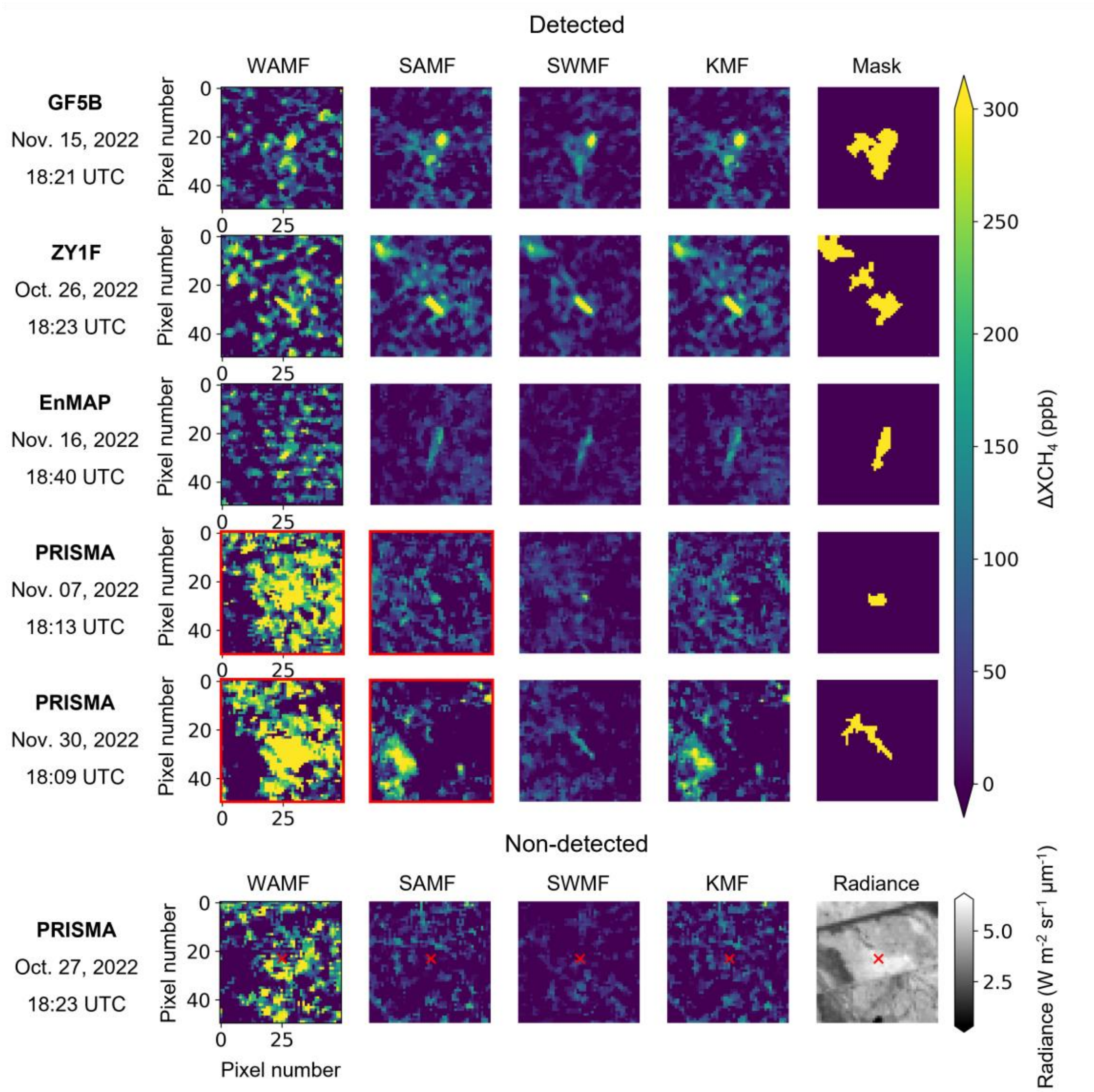

Figure 7. Maps of retrieved ΔXCH_4 from all six observations of four satellites for the 2022 experiment. Plumes from ground-level experimental emissions utilized by different methods and corresponding masks are listed in different columns. Panels enclosed in red borders indicate scenes where plume signals confuse with background noises. Retrievals of ΔXCH_4 and sensor-received radiance at 2300 nm are displayed separately for the PRISMA non-detected scene. Red cross symbols pinpoint the location of the emitter.

We then estimate the CH_4 emission flux rates from retrieved ΔXCH_4 maps using integrated mass enhancement (IME; Varon et al., 2018). Wind data is derived from Goddard Earth Observing System-Forward Processing (GEOS-FP; Molod et al., 2012). Metered-measurement of emission rate at the satellite overpassing time is represented using five-minute mean value. Figure 8 presents scatter plots illustrating the relationship between retrieved CH_4 emission flux rates and ground-based metered measurements. Notably, in the case of KMF, the slope of the fitted line for emission estimates is closest to 1 (0.95 for KMF), accompanied by the highest R-square (0.99 for KMF), the smallest RMSE (0.18 t/h for KMF, relative to metered measurements) and mean absolute error (MAE, 0.13 t/h for KMF, relative to metered measurements) values. The retrieval accuracy (inversely proportional to absolute difference between linear regression slope and 1:1 reference) for KMF is 13.1% higher than widely-used the SAMF method. Moreover, Figure 8 exhibits a more clustered distribution for KMF-based retrievals. Comparing with the SAMF method, R^2 increases 1.0%, while RMSE and MAE decrease 61.7% and 62.9%, respectively, for the KMF retrievals. This indicates the superior robustness on emission rate estimation when KMF is applied on different sensors. The linear regression slope of WAMF exceeds 1 (1.49 for WAMF), implying its trend for overestimation in emission rates. The WAMF method also exhibits the highest inversion uncertainty. Note that the WAMF-based emission rate estimations for data on October 21st and 27th, 2021 has a value of 6.7 and 5.9 t/h, which exceed the chart range, relative to metered-measurement of only 4.5 and 3.4 t/h. On the contrary, SAMF inversions demonstrate obvious underestimations for five PRISMA scenes due to missing plume signals. It results in a lower slope in the fitted line and more scattered distribution. For SWMF, the smaller STD value and slope suggest that its inversions are concentrated at levels below the true values. This distribution reflects a systematic underestimation of emission rates by the SWMF method. Compared to these single-channel retrieval methods, KMF exhibits higher accuracy and better multi-sensor stability.

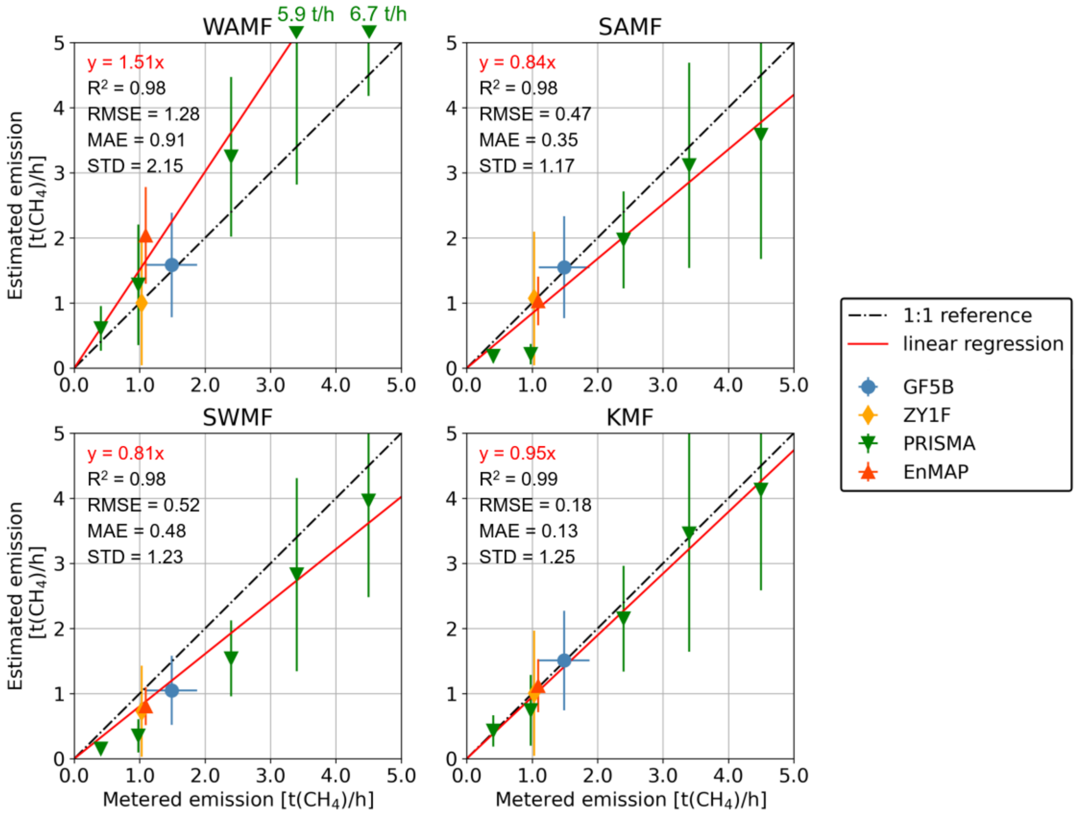

Figure 8. Estimated emission rates with GEOS-FP wind data versus metered measurement for WAMF, SAMF, SWMF, and KMF methods. Grey dashed lines represent 1:1 reference. Red lines represent the proportional fitting results obtained through the least squares method. Bars in x and y directions represent for uncertainty in metered-observing emission rates and retrieved emission rates, respectively. Uncertainties are too small to be visible except for GF5B, which passing time is one minute after the cessation of ground emission.

Further comparisons utilizing ground-based 10 m wind speeds are exhibited in Figure 9. It reveals that linear regression slopes for WAMF, SAMF, and KMF methods show an increase, with an elevated values falling in [0.07, 0.21]. The effective wind speed for the IME method is calculated by averaging the measured ground wind speeds 30 seconds before and after the satellite overpass. The standard deviation of the one-minute wind speed time series is used to compute the inversion uncertainty. For the five datasets employed in this study, the ground-based 10 m wind speed is on average increased by 0.86 m/s compared to the GEOS-FP reanalysis product, which also results in the elevation of the slope for all methods. Compared with using GEOS-FP wind data, the retrieval accuracy of SAMF increases 16.7%. The KMF method has an accuracy similar with SAMF, while RMSE and MAE decrease 71.4% and 70% compared to SAMF method at the same situation, respectively. Moreover, the wind speed STD constitutes a significant portion of the overall uncertainty in emission estimates (Gorroño et al., 2023). Thus, the low STD in metered wind speed measurements result in the reduction on CH_4 emission rate retrieval uncertainties for all methods, as shown in Figure 8. In addition, R^2 values for all methods increase when compared with GEOS-

FP-based results. The distributions of scatters are more centered around best fitted lines. This is due to lower relative σ of effective wind speed (defined as Duren et al., 2019) used for IME method on ground-based wind data (about 72.1% less). From Figure 8 and Figure 9, it is evident that the emission estimates from KMF still demonstrate superiority in accuracy when utilizing both reanalysis and ground-based wind speed data.

Furthermore, retrievals from both reanalysis and ground-measured wind data indicate that the measurements from GF5B and ZY1F closely align with the reference values for all methods. In contrast, the measurements from PRISMA and EnMAP are significantly influenced by the inversion methods. The KMF method has the capability to decrease the inversion bias in results of these two satellite instruments. Moreover, KMF also shows a better accuracy on retrieving emissions with low flux rates.

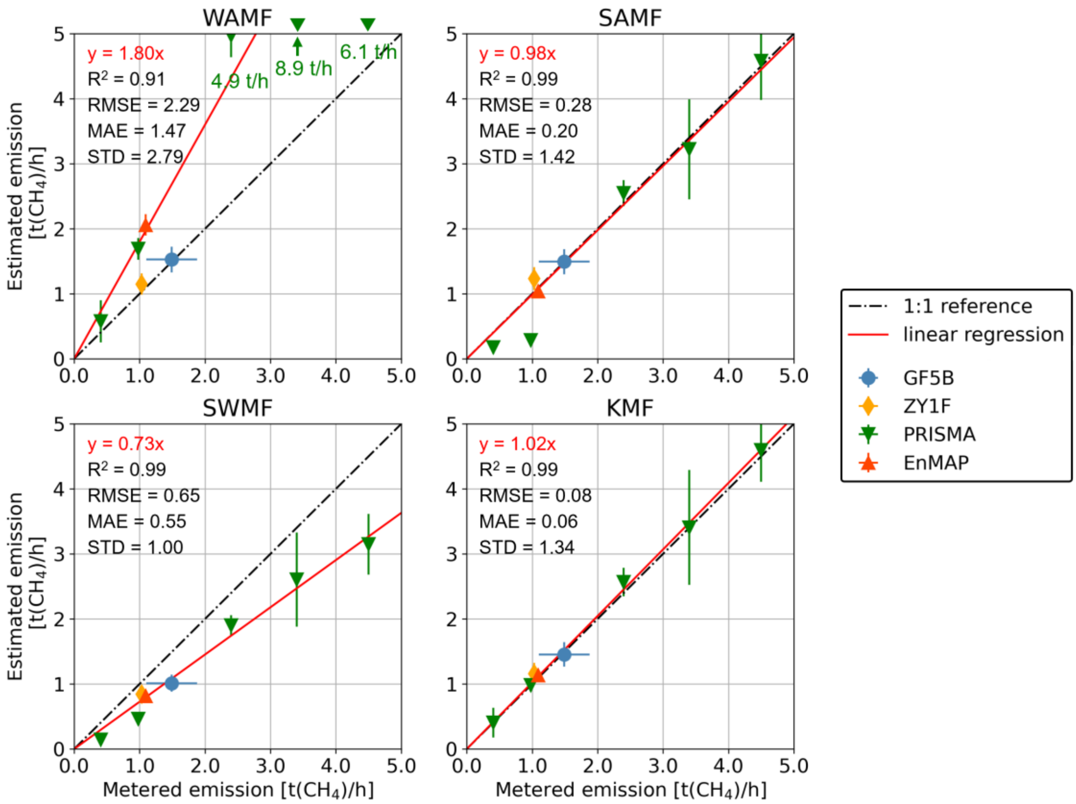

Figure 9. Estimated emission rates with locally measured wind data versus metered measurements for WAMF, SAMF, SWMF, and KMF, respectively. Bars in x and y directions represent for uncertainty in metered-observing emission rates and retrieved emission rates.

3.3 Emission-free scenario test for different sensors

In emission-free scenarios, noise typically adheres to a normal distribution. Therefore, the σ values of the statistical background distribution can serve as a measure of the magnitude of inversion precision (Irakulis-Loitxate et al., 2021). A smaller σ value indicates a higher retrieval precision.

For background analysis, we selected one scene of overpassing data on emission-free days for each satellite. 100×100-pixel subregions centered at the emitter of ground-controlling experiment are chosen to statistically fit the distribution of background ΔXCH_4 values, and σ values are then calculated. The results are illustrated in Figure 10. The retrieval precision (i.e., the σ value in the figure) for KMF method is 7.0-38.9 ppb lower than the SAMF results for different sensors, corresponding to 18.3-42.2% improvement. Note that the SWMF results exhibit lower σ values compared to the KMF results. As mentioned in Sec 3.1, this is attributed to the systematically lower values of ΔXCH_4 obtained by the SWMF method for background. This characteristic leads to a more tightly clustered distribution of pixel values.

In addition, Figure 10 also reveals the performance of different sensors. For the SAMF method, ZY1F exhibits the lowest inversion precision of 104.09 ppb, while GF5B demonstrates the highest. Similarly, for the KMF method, GF5B also shows the highest inversion performance, followed by EnMAP, ZY1F, and PRISMA. In addition, the KMF method demonstrates the most noticeable improvement in inversion precision on PRISMA data as outlined in Sec. 3.2. It is noteworthy that, for all four methods, the mean of fitted normal distribution for PRISMA background values exhibits a significant deviation from zero. This suggests the potentially systematic errors on ΔXCH_4 retrieval for the sensor of PRISMA. Such error may stem from drift between the actual spectral parameters of PRISMA and their nominal values. The impact of this systematic bias on ΔXCH_4 inversion has been discussed in Guanter et al. (2021).

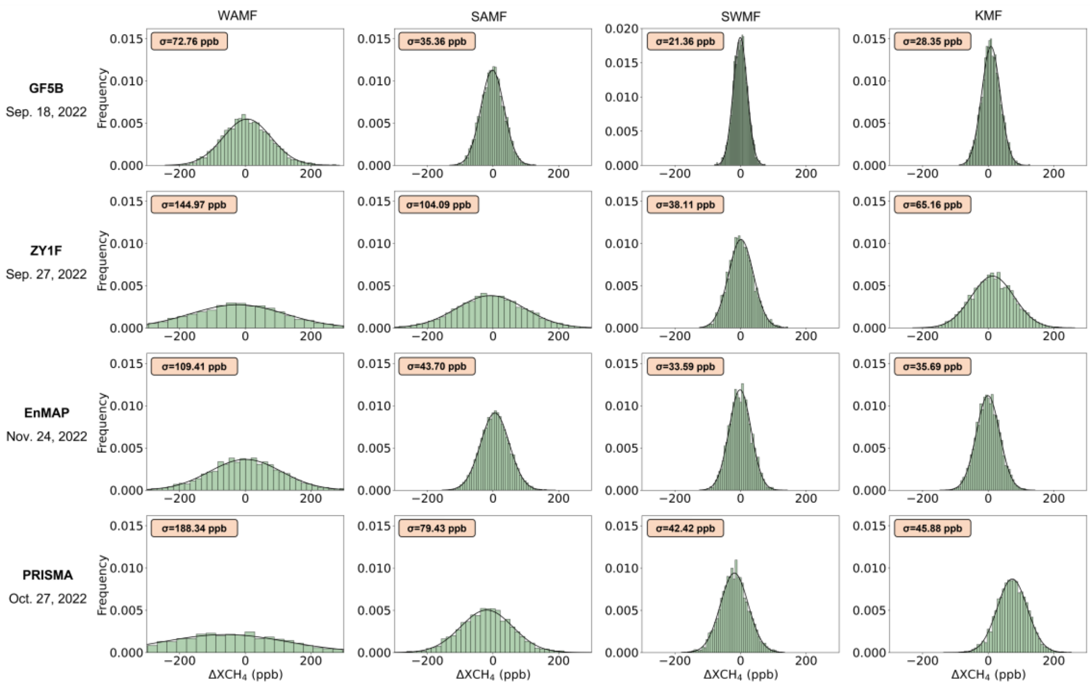

Figure 10. Histograms of the retrieved ΔXCH_4 inside selected 100×100-pixel subregions derived from different satellites and methods for emission-free scenarios. For each distribution, a Gaussian curve (black line) is fitted.

3.4 Method applications

In Figure 11, the application of the KMF method to analyze CH_4 emissions in two distinct real-world scenarios with varying surface conditions is presented. The results are compared with corresponding simulations from the WRF-LES model. Figures 11 (a) and 11 (b) depict emissions from oil and gas sources in the Delaware Basin, the United States, on February 9th, 2022. The surface condition is relatively flat for this scene. This emission is detected by the GF5B satellite. In Figures 11 (c) and 11 (d), CH_4 emissions from coal mines observed by the Gaofen 05 (GF5) satellite in Shanxi, China, on November 1, are shown. The surface condition in this region is more intricate, featuring anisotropic characteristics. When comparing the plume structures and their corresponding simulation results in these two scenarios, it becomes apparent that the spatial organization of the plumes is remarkably similar, and the concentration distributions closely match.

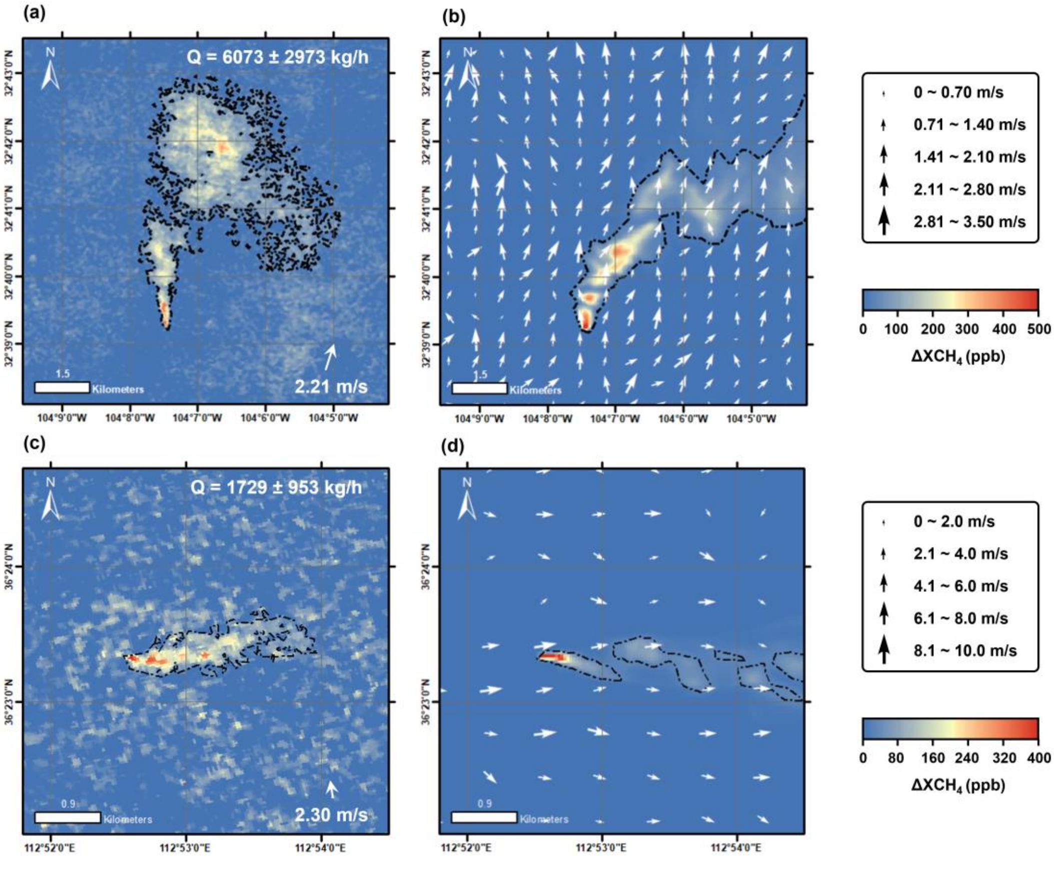

Figure 11. Retrieved ΔXCH_4 (first column) versus simulated results (second column) for plumes in (a and b) Delaware Basin, the US and (c and d) Shanxi, China. Reanalysis 10 m wind and retrieved CH_4 emission rates are presented for retrieval results. WRF-LES are run under an emission rate of 1000 kg/h, and the results are magnified to the retrieved emission rates by multiplying scaling factors. Model output wind fields are shown in white arrows. Aera within contour lines represent for pixels with ΔXCH_4 larger than 27 ppb (i.e., 1.5% of background concentration 1800 ppb).

Furthermore, we employ the KMF method for plume retrieval and CH_4 emission flux rate (Q in Figure 12) estimations using data from GF5 satellite series (GF5, GF5B, and GF5A). 16 CH_4 plumes emitted from energy industry in four regions around the world are identified, as illustrated in Figure 12. The analyzed plumes originate from the United States, Oman, Libya, and China, emitted by oil & gas facilities (in the US and Libya), power plants (in Oman), and coal mines (in China). The plumes are automatically extracted from background values using the mask strategy described in Sec. 3.2. For all selected cases, Q varies from 0.9 to 4.6 t CH_4 per hour derived with the KMF method. The largest emission source is located in Delaware basin, with an uncertainty of ±2.4 t/h in Q, while the smaller one in Libya with an uncertainty of ±0.3 t/h. Additionally, CH_4 plumes emitted from coal mines in the Shanxi region exhibit an aggregated pattern: six plumes are observed simultaneously within one scene. This clustering distribution of CH_4 plumes in the Shanxi region is attributed to the aggregation of coal mine sources within this area (Sheng et al., 2019).

Figure 13 illustrates the analysis of 16 emission cases using the KMF method. The results indicate that, compared to the traditional SAMF method, the KMF method estimates CH_4 emission flux rates with an average increase of 11.8%. This suggests that traditional MF methods may underestimate the mass of CH_4 emitted from point sources. Additionally, the estimated emission rates from WAMF and SWMF methods are overestimated by 41.8% and underestimated by 20.2%, respectively, compared to the SAMF method. This aligns with the trends observed in the method evaluation using ground truth values in Sec. 3.2.

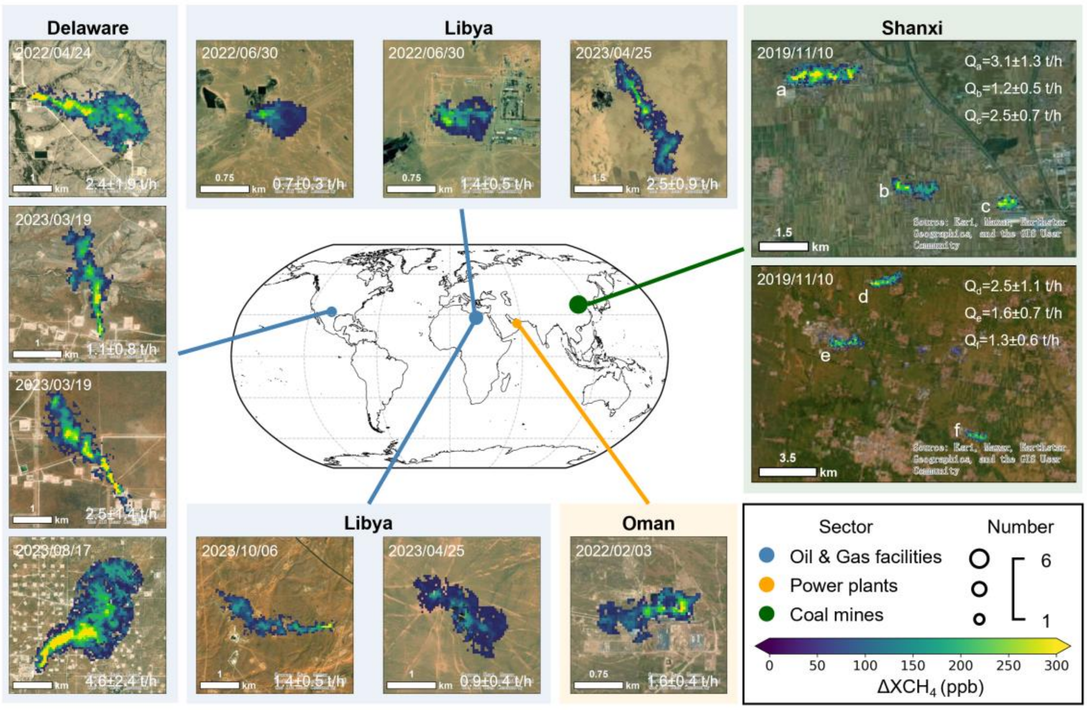

Figure 12. Spatial distribution, sectoral classification, and ΔXCH_4 maps of 16 casing plumes used in this study. Emitters locate in four regions of the world: the Delaware basin (U.S.), Libya, Oman, and Shanxi (China). Color and size of circles represent emitting sector and plume number, respectively. Retrieved plumes are superimposed on high-resolution true-color satellite images from the ESRI. Estimated Q values are presented for all plumes. White arrows show the directions of 10 m wind. UTC time of each plume is marked in the panel. Additionally, the median of emission

estimates obtained through the KMF algorithm closely aligns with that of SAMF while the former results exhibit a more median-concentrated distribution.

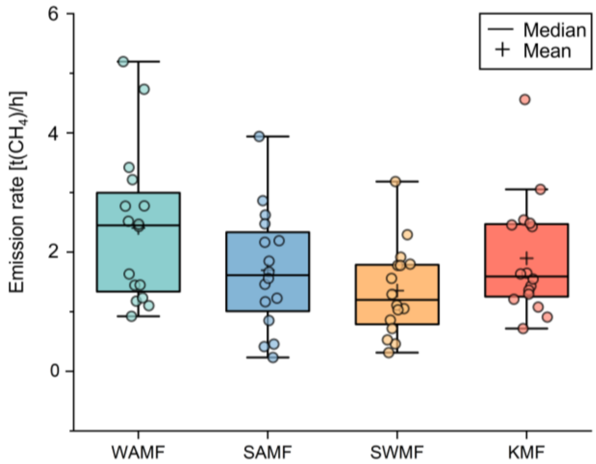

Figure 13. Box chart of estimated CH_4 emission rate retrieved from four methods of 16 plumes chosen for case study in Figure 11. Scatter plots illustrate estimated emission rates for 16 plume cases. Jitter has been applied along the x-axis to better show the data distribution.

4 Discussions and Conclusions

In this study, we developed a band fusion algorithm, KMF, to optimize the ΔXCH_4 and CH_4 emission flux rate inversions. Applying the Kalman filtering strategy, we estimated the band-dependent coefficients for each channel respectively and combined the inversion results linearly. An iteration process was added into the method to optimize the calculation of background radiance spectra. This algorithm integrates information from different CH_4 absorption channels, enabling more accurate ΔXCH_4 inversion and CH_4 emission flux rate estimation. Moreover, it mitigates the occurrence of false negatives associated with traditional MF algorithms. Thereby, KMF method enhances the monitoring capability for CH_4 point source leakage events.

Three-stage validation on this method have been conducted. We initially tested the algorithm using end-to-end simulation (Figure 6). The results indicate that KMF-retrieved ΔXCH_4 is about 30% closer to true values, while the variation is 20% less, when compared with the result derived from commonly-used SA window. Additionally, we verified the performance on quantifying the CH_4 emission flux rate of KMF using ground metered-measurements (Figure 7, 8, and 9). It substantiates an approximately 13% improvement on emission rate estimation accuracy for KMF method compared with SAMF method when using both reanalysis and ground-observed wind data. The robustness for multi-sensor retrieval revealed by our results also enables wider application for KMF method. Finally, emission-free scenarios from ground-controlling experiment are employed to test the method precision (Figure 10). An average enhancement of 21.9 ppb in ΔXCH_4 retrieval precision is exhibited when utilizing the KMF method. These validations suggest that the KMF method can utilize spectral information from various channels to constrain and refine the inversion of ΔXCH_4, leading to more accurate estimates on CH_4 emission rates. Further application of KMF method on 16 CH_4 plumes all over the world (Figure 12 and 13) indicate an approximately 12% underestimation on CH_4 emission rates of traditional SAMF.

This study is dedicated to the development of a multi-channel MF algorithm designed to improve the retrieval accuracy for ΔXCH_4 and emission rate. The current algorithm presently decreases the interference from retrieval noises by the linear combination of multi-channel results. However, in real-world applications, some bias requires non-linear calibration (e.g., error induced by spectral nonuniformity; Guanter et al., 2009). This nonuniformity is determined by specific satellite sensors, which non-linearly influence the MF results across different spectral channels by affecting the actual spectral properties such as central wavelength and FWHM. Such deviations could lead to additional systematic bias for KMF method. Further work is needed to consider the non-linear calibration in the KMF algorithm, increasing the overall retrieval accuracy across numerous satellite platforms.

In summary, the KMF method proposed in this study effectively addresses the issues of plume signal missing, and underestimation of CH_4 emission flux rates encountered by traditional MF algorithms. Our results indicate that the KMF method holds significant potential for application in multi-satellite coordinated monitoring of CH_4 point source emissions. It can provide more accurate CH_4 column concentrations and emission flux estimates for emitting events, offering precise observational support for top-down CH_4 accounting in key regions globally.

Declaration of interests

The authors declare that they have no known competing financial interests or personal relationships that could have appeared to influence the work reported in this paper.

Declaration of Competing Interest

None.

Acknowledgments

This work is funded by National Key Research and Development Program of China (2022YFE0209100). We would like to thank the China Centre for Resources Satellite Data and Application for the GF5 series and ZY1F data. Thanks are also extended to the Italian Space Agency and the Space Agency of the German Aerospace Center for sharing the PRISMA and the EnMAP data used in this study. Further, the authors would like to acknowledge Evan D. Sherwin, Adam R. Brandt and other members in Stanford controlled-releasing experiment team for generously providing the ground-measured data. These valuable contributions significantly enriched the data

resources and supported the successful execution of this research project.

Reference

Ayasse, A.K., Cusworth, D., O'Neill, K., Fisk, J., Thorpe, A.K., Duren, R., 2023. Performance and sensitivity of column-wise and pixel-wise methane retrievals for imaging spectrometers. Atmos Meas Tech 16, 6065–6074. https://doi.org/10.5194/amt-16-6065-2023.

Berk, A., Conforti, P., Kennett, R., Perkins, T., Hawes F. and van den Bosch, J., 2014. MODTRAN® 6: A major upgrade of the MODTRAN® radiative transfer code, in: 2014 6th workshop on hyperspectral image and signal processing: evolution in remote sensing (whispers), Workshop on Hyperspectral Image and Signal Processing. IEEE, 345 E 47th St., New York, NY 10017 USA. https://doi.org/10.1109/WHISPERS.2014.8077573.

Brandt, A.R., Heath, G.A., Kort, E.A., O'Sullivan, F., Pétron, G., Jordaan, S.M., Tans, P., Wilcox, J., Gopstein, A.M., Arent, D., Wofsy, S., Brown, N.J., Bradley, R., Stucky, G.D., Eardley, D., Harriss, R., 2014. Methane leaks from north American natural gas systems. Science (1979) 343, 733–735. https://doi.org/10.1126/science.1247045.

Cogliati, S., Sarti, F., Chiarantini, L., Cosi, M., Lorusso, R., Lopinto, E., Miglietta, F., Genesio, L., Guanter, L., Damm, A., Pérez-López, S., Scheffler, D., Tagliabue, G., Panigada, C., Rascher, U., Dowling, T.P.F., Giardino, C., Colombo, R., 2021. The PRISMA imaging spectroscopy mission: overview and first performance analysis. Remote Sens Environ 262, 112499. https://doi.org/10.1016/j.rse.2021.112499.

Duren, R.M., Thorpe, A.K., Foster, K.T., Rafiq, T., Hopkins, F.M., Yadav, V., Bue, B.D., Thompson, D.R., Conley, S., Colombi, N.K., Frankenberg, C., McCubbin, I.B., Eastwood, M.L., Falk, M., Herner, J.D., Croes, B.E., Green, R.O., Miller, C.E., 2019. California's methane super-emitters. Nature 575, 180-+. https://doi.org/10.1038/s41586-019-1720-3.

Foote, M.D., Dennison, P.E., Sullivan, P.R., O'Neill, K.B., Thorpe, A.K., Thompson, D.R., Cusworth, D.H., Duren, R., Joshi, S.C., 2021. Impact of scene-specific enhancement spectra on matched filter greenhouse gas retrievals from imaging spectroscopy. Remote Sens Environ 264. https://doi.org/10.1016/j.rse.2021.112574.

Foote, M.D., Dennison, P.E., Thorpe, A.K., Thompson, D.R., Jongaramrungruang, S., Frankenberg, C., Joshi, S.C., 2020. Fast and accurate retrieval of methane concentration from imaging spectrometer data using sparsity prior. IEEE Transactions on Geoscience and Remote Sensing 58, 6480–6492. https://doi.org/10.1109/TGRS.2020.2976888

Gorroño, J., Varon, D.J., Irakulis-Loitxate, I., Guanter, L., 2023. Understanding the potential of Sentinel-2 for monitoring methane point emissions. Atmos Meas Tech 16, 89–107. https://doi.org/10.5194/amt-16-89-2023.

Guanter, L., Irakulis-Loitxate, I., Gorroño, J., Sánchez-García, E., Cusworth, D.H., Varon, D.J., Cogliati, S., Colombo, R., 2021. Mapping methane point emissions with the PRISMA spaceborne imaging spectrometer. Remote Sens Environ 265. https://doi.org/10.1016/j.rse.2021.112671.

Guanter, L., Richter, R., Moreno, J., 2006. Spectral calibration of hyperspectral imagery using atmospheric absorption features. Appl. Opt. 45, 2360–2370. https://doi.org/10.1364/AO.45.002360.

Guanter, L., Segl, K., Sang, B., Alonso, L., Kaufmann, H., Moreno, J., 2009. Scene-based spectral calibration assessment of high spectral resolution imaging spectrometers. Opt. Express 17, 11594–11606. https://doi.org/10.1364/OE.17.011594.

Hönninger, G., von Friedeburg, C., Platt, U., 2004. Multi axis differential optical absorption spectroscopy (MAX-DOAS). Atmos Chem Phys 4, 231–254. https://doi.org/10.5194/acp-4-231-2004.

Irakulis-Loitxate, I., Guanter, L., Liu, Y.-N., Varon, D.J., Maasakkers, J.D., Zhang, Yuzhong, Chulakadabba, A., Wofsy, S.C., Thorpe, A.K., Duren, R.M., Frankenberg, C., Lyon, D.R., Hmiel, B., Cusworth, D.H., Zhang, Yongguang, Segl, K., Gorroño, J., Sánchez-García, E., Sulprizio, M.P., Cao, K., Zhu, H., Liang, J., Li, X., Aben, I., Jacob, D.J., 2021. Satellite-based survey of extreme methane emissions in the Permian basin. Sci Adv 7, eabf4507. https://doi.org/10.1126/sciadv.abf4507.

Kalman, R.E., 1960. A new approach to linear filtering and prediction problems. ASME. J. Basic Eng. March 1960; 82(1): 35–45. https://doi.org/10.1115/1.3662552.

Kirschke, S., Bousquet, P., Ciais, P., Saunois, M., Canadell, J.G., Dlugokencky, E.J., Bergamaschi, P., Bergmann, D., Blake, D.R., Bruhwiler, L., Cameron-Smith, P., Castaldi, S., Chevallier, F., Feng, L., Fraser, A., Heimann, M., Hodson, E.L., Houweling, S., Josse, B., Fraser, P.J., Krummel, P.B., Lamarque, J.F., Langenfelds, R.L., Le Quéré, C., Naik, V., O'Doherty, S., Palmer, P.I., Pison, I., Plummer, D., Poulter, B., Prinn, R.G., Rigby, M., Ringeval, B., Santini, M., Schmidt, M., Shindell, D.T., Simpson, I.J., Spahni, R., Steele, L.P., Strode, S.A., Sudo, K., Szopa, S., van der Werf, G.R., Voulgarakis, A., van Weele, M., Weiss, R.F., Williams, J.E., Zeng, G., 2013. Three decades of global methane sources and sinks. Nat Geosci 6, 813–823. https://doi.org/10.1038/NGEO1955.

Kort, E.A., Frankenberg, C., Costigan, K.R., Lindenmaier, R., Dubey, M.K., Wunch, D., 2014. Four corners: The largest US methane anomaly viewed from space. Geophys Res Lett 41, 6898–6903. https://doi.org/10.1002/2014GL061503.

Lyon, D.R., Zavala-Araiza, D., Alvarez, R.A., Harriss, R., Palacios, V., Lan, X., Talbot, R., Lavoie, T., Shepson, P., Yacovitch, T.I., Herndon, S.C., Marchese, A.J., Zimmerle, D., Robinson, A.L., Hamburg, S.P., 2015. Constructing a spatially resolved methane emission inventory for the Barnett Shale region. Environ Sci Technol 49, 8147–8157. https://doi.org/10.1021/es506359c.

Maasakkers, J.D., Omara, M., Gautam, R., Lorente, A., Pandey, S., Tol, P., Borsdorff, T., Houweling, S., Aben, I., 2022. Reconstructing and quantifying methane emissions from the full duration of a 38-day natural gas well blowout using space-based observations. Remote Sens Environ 270, 112755. https://doi.org/10.1016/j.rse.2021.112755.

Manolakis, D., Truslow, E., Pieper, M., Cooley, T., Brueggeman, M., 2013. Detection algorithms in hyperspectral imaging systems: An overview of practical algorithms. IEEE Signal Process Mag 31, 24–33. https://doi.org/10.1109/MSP.2013.2278915.

Molod, A., Takacs, L., Suarez, M., Bacmeister, J., Song, I.-S., Eichmann, A., 2012. The GEOS-5 atmospheric general circulation model: Mean climate and development from MERRA to Fortuna (No. GSFC. TM. 01153.2012).

Montzka, S.A., Dlugokencky, E.J., Butler, J.H., 2011. Non-CO_2 greenhouse gases and climate change. Nature 476, 43–50. https://doi.org/10.1038/nature10322.

Pandey, S., Gautam, R., Houweling, S., van der Gon, H.D., Sadavarte, P., Borsdorff, T., Hasekamp, O., Landgraf, J., Tol, P., van Kempen, T., Hoogeveen, R., van Hees, R., Hamburg, S.P., Maasakkers, J.D., Aben, I., 2019. Satellite observations reveal extreme methane leakage from a natural gas well blowout. Proc Natl Acad Sci U S A 116, 26376–26381.

https://doi.org/10.1073/pnas.1908712116.

Pei, Z.P., Han, G., Mao, H.Q., Chen, C.H., Shi, T.Q., Yang, K.Y., Ma, X., Gong, W., 2023. Improving quantification of methane point source emissions from imaging spectroscopy. Remote Sens Environ 295. https://doi.org/10.1016/j.rse.2023.113652.

Roger, J., Guanter, L., Gorroño, J., Irakulis-Loitxate, I., 2023a. Exploiting the entire near-infrared spectral range to improve the detection of methane plumes with high-resolution imaging spectrometers. Atmos. Meas. Tech. Discuss. 2023, 1–21. https://doi.org/10.5194/amt-2023-168.

Roger, J., Irakulis-Loitxate, I., Valverde, A., Gorroño, J., Chabrillat, S., Brell, M., Guanter, L., 2023b. High-resolution methane mapping with the EnMAP satellite imaging spectroscopy mission. IEEE Transactions on Geoscience and Remote Sensing, https://doi.org/10.1109/TGRS.2024.3352403.

Shen, L., Jacob, D.J., Gautam, R., Omara, M., Scarpelli, T.R., Lorente, A., Zavala-Araiza, D., Lu, X., Chen, Z., Lin, J., 2023. National quantifications of methane emissions from fuel exploitation using high resolution inversions of satellite observations. Nat Commun 14, 4948. https://doi.org/10.1038/s41467-023-40671-6.

Sheng, J., Song, S., Zhang, Y., Prinn, R.G., Janssens-Maenhout, G., 2019. Bottom-up estimates of coal mine methane emissions in China: a gridded inventory, emission factors, and trends. Environ Sci Technol Lett 6, 473–478. https://doi.org/10.1021/acs.estlett.9b00294.

Sherwin, E., El Abbadi, S., Burdeau, P., Zhang, Z., Chen, Z., Rutherford, J., Chen, Y., Brandt, A., 2023a. Single-blind test of nine methane-sensing satellite systems from three continents. EGUsphere 2023, 1. https://doi.org/10.31223/x56089.

Sherwin, E.D., Rutherford, J.S., Chen, Y., Aminfard, S., Kort, E.A., Jackson, R.B., Brandt, A.R., 2023b. Single-blind validation of space-based point-source detection and quantification of onshore methane emissions. Sci Rep 13. https://doi.org/10.1038/s41598-023-30761-2.

Song, Q., Ma, C., Liu, J., Wei, H., 2022. Quantifying ocean surface green tides using high-spatial resolution thermal images. Opt. Express 30, 36592–36602. https://doi.org/10.1364/OE.472479.

Storch, T., Honold, H.-P., Chabrillat, S., Habermeyer, M., Tucker, P., Brell, M., Ohndorf, A., Wirth, K., Betz, M., Kuchler, M., Mühle, H., Carmona, E., Baur, S., Mücke, M., Löw, S., Schulze, D., Zimmermann, S., Lenzen, C., Wiesner, S., Aida, S., Kahle, R., Willburger, P., Hartung, S., Dietrich, D., Plesia, N., Tegler, M., Schork, K., Alonso, K., Marshall, D., Gerasch, B., Schwind, P., Pato, M., Schneider, M., de los Reyes, R., Langheinrich, M., Wenzel, J., Bachmann, M., Holzwarth, S., Pinnel, N., Guanter, L., Segl, K., Scheffler, D., Foerster, S., Bohn, N., Bracher, A., Soppa, M.A., Gascon, F., Green, R., Kokaly, R., Moreno, J., Ong, C., Sornig, M., Wernitz, R., Bagschik, K., Reintsema, D., La Porta, L., Schickling, A., Fischer, S., 2023. The EnMAP imaging spectroscopy mission towards operations. Remote Sens Environ 294, 113632. https://doi.org/10.1016/j.rse.2023.113632.

Thompson, D.R., Leifer, I., Bovensmann, H., Eastwood, M., Fladeland, M., Frankenberg, C., Gerilowski, K., Green, R.O., Kratwurst, S., Krings, T., Luna, B., Thorpe, A.K., 2015. Real-time remote detection and measurement for airborne imaging spectroscopy: a case study with methane. Atmos Meas Tech 8, 4383–4397. https://doi.org/10.5194/amt-8-4383-2015.

Thompson, D.R., Thorpe, A.K., Frankenberg, C., Green, R.O., Duren, R., Guanter, L., Hollstein, A., Middleton, E., Ong, L., Ungar, S., 2016. Space-based remote imaging spectroscopy of the

Aliso Canyon CH_4 superemitter. Geophys Res Lett 43, 6571–6578. https://doi.org/10.1002/2016GL069079.

Thorpe, A.K., Frankenberg, C., Aubrey, A.D., Roberts, D.A., Nottrott, A.A., Rahn, T.A., Sauer, J.A., Dubey, M.K., Costigan, K.R., Arata, C., Steffke, A.M., Hills, S., Haselwimmer, C., Charlesworth, D., Funk, C.C., Green, R.O., Lundeen, S.R., Boardman, J.W., Eastwood, M.L., Sarture, C.M., Nolte, S.H., Mccubbin, I.B., Thompson, D.R., McFadden, J.P., 2016. Mapping methane concentrations from a controlled release experiment using the next generation airborne visible/infrared imaging spectrometer (AVIRIS-NG). Remote Sens Environ 179, 104–115. https://doi.org/10.1016/j.rse.2016.03.032.

Thorpe, A.K., Green, R.O., Thompson, D.R., Brodrick, P.G., Chapman, J.W., Elder, C.D., Irakulis-Loitxate, I., Cusworth, D.H., Ayasse, A.K., Duren, R.M., Frankenberg, C., Guanter, L., Worden, J.R., Dennison, P.E., Roberts, D.A., Chadwick, K.D., Eastwood, M.L., Fahlen, J.E., Miller, C.E., 2023. Attribution of individual methane and carbon dioxide emission sources using EMIT observations from space. Sci Adv 9, eadh2391. https://doi.org/10.1126/sciadv.adh2391.

Thorpe, A.K., Roberts, D.A., Bradley, E.S., Funk, C.C., Dennison, P.E., Leifer, I., 2013. High resolution mapping of methane emissions from marine and terrestrial sources using a Cluster-Tuned Matched Filter technique and imaging spectrometry. Remote Sens Environ 134, 305–318. https://doi.org/10.1016/j.rse.2013.03.018.

Varon, D.J., Jacob, D.J., Jervis, D., McKeever, J., 2020. Quantifying time-averaged methane emissions from individual coal mine vents with GHGSat-D satellite observations. Environ Sci Technol 54, 10246–10253. https://doi.org/10.1021/acs.est.0c01213.

Varon, D.J., Jacob, D.J., McKeever, J., Jervis, D., Durak, B.O.A., Xia, Y., Huang, Y., 2018. Quantifying methane point sources from fine-scale satellite observations of atmospheric methane plumes. Atmos Meas Tech 11, 5673–5686. https://doi.org/10.5194/amt-11-5673-2018.

Varon, D.J., McKeever, J., Jervis, D., Maasakkers, J.D., Pandey, S., Houweling, S., Aben, I., Scarpelli, T., Jacob, D.J., 2019. Satellite discovery of anomalously large methane point sources from oil/gas production. Geophys Res Lett 46, 13507–13516. https://doi.org/10.1029/2019GL083798.

Appendix

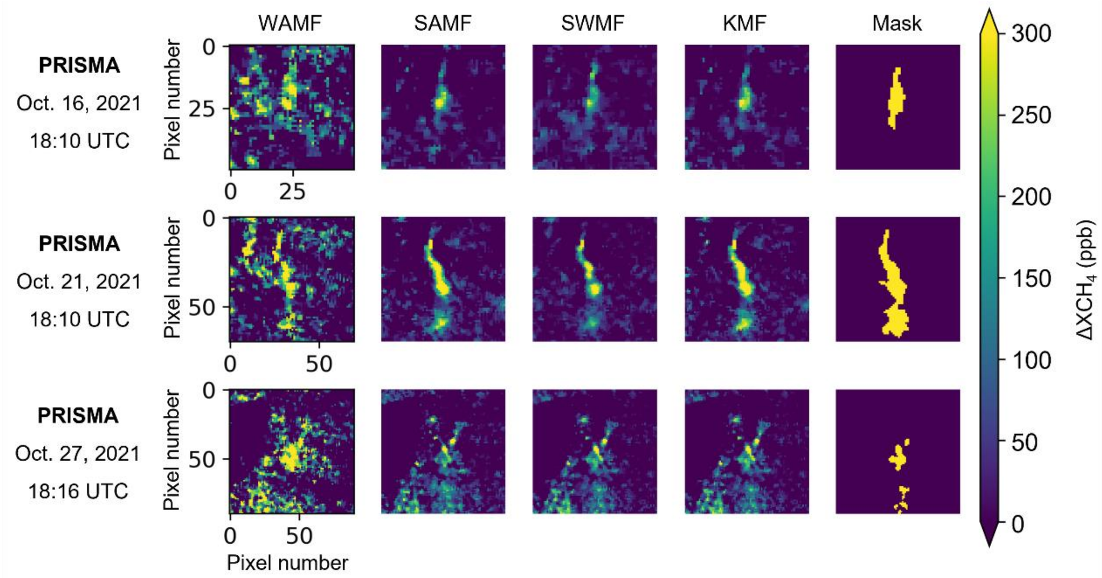

Figure S1. Maps of retrieved ΔXCH_4 from all three observations of PRISMA for 2021 experiment. Plumes from ground-level experimental emissions utilized by different methods and corresponding masks are listed in different columns.